Indonesian Physical Review
Volume 4 Issue 1, January 2021
P-ISSN: 2615-1278, E-ISSN: 2614-7904

Particles Size and Lattice Strain Effect on the Optical Constants of Fe_3O_4 Nanoparticles

I Putu Tedy Indrayana[1,2]*, Margaretha Tabita Tuny[3]
[1]*Physics Study Program, Universitas Halmahera, Indonesia.*
[2]*Physics Study Program, Universitas Udayana, Indonesia. E-mail*: tedyindrayana@gmail.com*
[3]*Forestry Study Program, Universitas Halmahera, Indonesia. E-mail: tabitatuny@yahoo.com*

ARTICLE INFO

Article History:
Received: 10-01-2021
Revised: 07-02-2021
Accepted: 11-02-2021

Keywords :
Lattice strain; Optical constants; Particles Size

How To Cite :
Indrayana, I P.T., Tuny, M.T (2020). Particles Size and Lattice Strain Effect on the Optical Constant of Fe_3O_4 Nanoparticles. Indonesian Physical Review, 4(1), 23-42

DOI :
https://doi.org/10.29303/ipr.v4i1.71

ABSTRACT

In the case of optical sensors such as the Surface Plasmon Resonance (SPR) sensor, the Fe_3O_4 nanoparticles play a role to boost the signal however they can increase the detection sensitivity of the biosensor. For this application, the optical properties of Fe_3O_4 nanoparticles need to be studied. The optical properties are described in terms of their optical constants. Therefore, this work was purposed to study the effect of the particle size and lattice strain on the optical constants of Fe_3O_4 nanoparticles. Samples were synthesized by using the coprecipitation technique. Two calcination temperatures, i.e., 150°C and 250°C for 4 hours were applied to the samples. Samples were characterized for their diffraction pattern and optical properties by using XRD and Specular UV-Vis Spectroscopy technique, consecutively. The particle size and lattice strain were estimated by using the Williamson-Hall (W-H) method. The effect of the particle size and their optical constants on the reflectance curve in the SPR sensor application was also performed toward a simulation by using Winspall 3.02 software. The results show that calcination temperature causes an increase in particle size and a decrease in lattice strain. The optical constants, such as absorbance (A), absorption coefficient (α), extinction coefficient (k), refractive index (n), dielectric constants (ε), optical conductivity (σ), and the Urbach energy (Eu) significantly depended on particles size and lattice strain. However, the particle size and optical constant were significantly influent the SPR angle in the reflectance curve of Fe_3O_4.

Introduction

Up to this time, various types of ferroic material are still massively being studied by researchers due to their fascinating physical and chemical properties. Among those materials, Fe_3O_4 gets tremendous attention due to its unique structural properties. The Fe_3O_4 nanoparticle has a cubic inverse spinel structure [1]. The structure has two different crystallographic sites, e.g., tetrahedral and octahedral oxygen coordination sites. These sites are occupied by divalent and three valent metal cations (Fe^{2+} and Fe^{3+}). The Fe^{2+} cations occupy octahedral sites, while Fe^{3+} cations fully occupy tetrahedral sites and some also in octahedral [2]. The distribution of cations between these sites and their exchange interaction

provide superior optical, electrical, electronic, and magnetic properties. Since, those properties allow the Fe_3O_4 having numerous potential applications, for instant complex targeted drug delivery and boron-neutron capture therapy [3], cancer drug loader [4], drug vehicle for central nervous system treatment [5], magnetic particle imaging (IMP) in the magnetic resonance imaging (MRI) system [6], adsorbent for heavy metals [7,8], antimicrobial and photocatalyst material [9], electromagnetic wave absorber [10], coating materials for the anode of the Li-ion battery [11], and nanotag in biosensors [12–15]. In short, the properties of the Fe_3O_4 strongly depend on their structure. Moreover, in nanoscale, the quantum confinement effect also occurs. The properties of Fe_3O_4 also depend on the size of the particles.

The size of the nanoparticle can be controlled via the preparation of samples. Sample of Fe_3O_4 nanoparticles can be prepared using "top-down" and "bottom-up" approaches. The top-down approach includes photolithography, high-energy–ball milling, and grinding [16]. Meanwhile, the bottom-up approach includes pyrolysis [6], microemulsion [17], hydrothermal and solvothermal [1,18], thermal decomposition, sol-gel [14], solid-state reaction, sonochemical auto combustion, microwave-assisted synthesis [19], chemical coprecipitation [20,21], and biosynthesis [6]. Among those methods, chemical coprecipitation has been used extensively due to its simple procedure, the efficiency of energy usage, not time-consuming, doesn't need additional chemical reagents, except hydroxide compound (as co-precipitator) and hydrochloric acid (as oxydator), and having high yield so that it is very beneficial for industrial-scale production. However, this method has some drawbacks, i.e., wide range distribution of the particle size, smaller particle size which allows them to experience agglomeration after synthesis, low crystallinity due to low ordered crystallites, non-homogenous shape, low dispersibility of the particles in a solvent, such water, and probably the sample consists of extra phases likes hematite and maghemite [5,6,16,17]. Moreover, since the particle size of the Fe_3O_4 nanoparticles depends on the preparation method, then any synthesis parameters, such as reaction temperature, precursor types and concentrations, pH, and reaction rate should be controlled [6,16,17,22]. Additionally, extra treatment to the synthesized nanoparticles such as calcination is also able to be given.
In this work, we focus on the study of particle size and lattice strain effect on the optical constants of Fe_3O_4 nanoparticles.

According to the literature review, the lack of papers provided a comprehensive discussion about the optical properties of the Fe_3O_4 related to their application in surface plasmon resonance (SPR) based sensor. Some papers only provided part by a part discussion concerning to one or some optical properties (see Table 1). Any physical information about the optical properties of Fe_3O_4 in terms of the nanoscale point of view is really important. Therefore, this work is purposed to provide a comprehensive and deeper discussion about those optical constants. The optical constants are very urgent for their application in an optical sensor system, for instant SPR-based sensor. Furthermore, this work also provides brief simulation results about the application of Fe_3O_4 nanoparticles as a dielectric layer in the SPR-sensor system.

Table 1. Literatures related to the synthesis and characterization of the optical properties of Fe_3O_4.

Type of Materials	***Type of Precursors***	***Synthesis Method***	***Synthesis Temp. (°C)***	***Extra Treatment***	***Particle Size (nm)***	***Optical Properties***	***Ref.***
Fe_3O_4	Metal nitrate ($Fe(NO_3)_3.9H_2O$) & fuel urea ($CO(NH_2)_2$)	Facile microwave combustion	-	Calcination at 500°C	20 - 35	Optical gap energy (2.05 eV – 2.12 eV)	[19]
Fe_3O_4	$Fe_2SO_4.7H_2O$ & Ethylene Glycol	Reflux under N-atmosphere	50	Annealing at 300°C, 400°C, and 500°C	20 – 25	Absorbance	[23]
Fe_3O_4 incorpora-ted in the Er^{3+} doped tellurite glasses	Iron sand	Dry Milling	-	Annealing at 300°C	18 - 70	Absorbance, Optical energy band gap (2.1 eV – 3.3 eV), & Urbach energy (0.16 eV – 0.30 eV)	[24]
Fe_3O_4	Ferrous chloride hexahydrate ($FeCl_2.6H_2O$) & Ferric chloride ($FeCl_3.6H_2O$)	Coprecipita-tion	80	Annealing at 230°C	11.3 – 35.9	Absorbance & Optical gap energy (0.53 eV– 3.32 eV)	[25]
Fe_3O_4	Metal nitrate ($Fe(NO_3)_3.9H_2O$)	Chemical	75	-	56.61 – 111.22	Transmittance, Reflection, Refractive index, Optical gap energy, Optical conductivity, & Extinction coefficient	[26]
Fe_3O_4	Ferrous chloride hexahydrate ($FeCl_2.6H_2O$) & Ferric chloride ($FeCl_3.6H_2O$)	Coprepita-tion	55	Addition of organic modifier (PVP, sodium citrate, tartaric acid, ethylene glycol & dextrin)	2.9 – 12.2	Absorbance & Optical gap energy (2.51 eV – 3.	[27]
Fe_3O_4/PVP	Ferrous chloride tetrahydrate ($FeCl_2.4H_2O$), Ferric chloride hexahydrate ($FeCl_3.6H_2O$), & Polyvinylpyrroli-done (PVP) $(C_6H_9NO)_n$	Coprecipita-tion	90		6.69 – 8.77	Dielectric constant & Conductivity	[28]
Fe_3O_4	Iron sand	Coprecipita-tion	80	Calcination at 150°C & 250°C for 2 – 4 hours	14.84 – 24.90	Absorbance & Optical gap energy	[29]
Fe_3O_4/Ag	Metal nitrate ($Fe(NO_3)_3.9H_2O$) & $AgNO_3$	Thermal decomposi-tion	240	-	8.2 – 9.0	Magneto-optical	[30]
Fe_3O_4	Ferrous chloride	Coprecipita	90	-	10.70 –	Absorbance &	[31]

Type of Materials	*Type of Precursors*	*Synthesis Method*	*Synthesis Temp. (°C)*	*Extra Treatment*	*Particle Size (nm)*	*Optical Properties*	*Ref.*
	tetrahydrate ($FeCl_2.4H_2O$), Ferric chloride hexahydrate ($FeCl_3.6H_2O$), & NH_4OH	-tion under N_2 gases bubbling			30.43	Optical gap energy (1.47 eV – 1.84 eV)	

Theory and Calculation

Williamson-Hall Method for Estimation Particle Size and Lattice Strain:

Williamson-Hall method or well-known as the W-H method is a method for estimating the particle size and lattice strain of the nanoscale particle (crystalline materials) according to the diffraction pattern. Accordingly, the diffraction peak broadening of the nanoscale particle is not only attributed to particle size but also lattice strain and defect [32–37]. Therefore, the contribution of the strain-induced deformation broadening on the diffraction peak has also needed to be considered. Hence, the total integral breadth of a Bragg peak or FWHM (*full width at half maximum*) is the addition between peak width due to strain β_{strain} and particle size β_{size}, such as represented by (1),

$$\beta_{hkl} = \beta_{size} + \beta_{strain} \quad (1)$$

Peak broadening due to particle size can be determined from the Scherrer equation such as (2),

$$\beta_{size} = \frac{k\lambda}{t\cos\theta_{hkl}} \quad (2)$$

where k is a shape factor (0.89 for nearly spherical particle), λ is an X-ray wavelength (0.15405980 nm), t is particle size (nm), and θ_{hkl} is the diffraction angle of the corresponding peak with a plane (hkl) [35]. Meanwhile, peak broadening due to lattice strain can be determined by using (3),

$$\beta_{strain} = \varepsilon(4\tan\theta_{hkl}) \quad (3)$$

where ε is the lattice strain [35].

Therefore, the Willamson-Hall equation can be rewritten as follows,

$$\beta_{hkl} = \frac{k\lambda}{t\cos\theta_{hkl}} + \varepsilon(4\tan\theta_{hkl}) \quad (4)$$

or by doing a little mathematical manipulation, so (4) can be expressed as,

$$\beta_{hkl}\cos\theta_{hkl} = \frac{k\lambda}{t} + \varepsilon(4\sin\theta_{hkl}) \quad (5)$$

This equation represents a uniform deformation model (UDM), in which the crystalline material is assumed to be isotropic and the strain uniformly distributed in all directions of the crystal.

By plotting sin θ_{hkl} (x-axis) versus β_{hkl} cos θ_{hkl} (y-axis) for all investigated diffraction peaks, so the average particle size and the lattice strain can be estimated by the y-intercept extrapolation and the slope of the linear fitting line, as follow,

$$t = \frac{k\lambda}{y\text{ - intercept}} \quad (6)$$

$$\varepsilon = \frac{\text{slope}}{4} \tag{7}$$

Optical Properties of Nanoparticles:

The optical properties of nanoparticles are determined by how the interaction between electromagnetic waves (light) and the nanoparticles. When a light beam interacts with nanoparticles, so some optical phenomena might occurred, e.g., reflection, propagation, and transmission (see Figure 1). Some of the light beams will be reflected from the surface of the nanoparticles, while the rest enters the nanoparticles and propagates through them. The propagated light through the nanoparticles might be reflected again by their back surface. If during the propagation through nanoparticles, the frequency of the light beam is resonant with transition frequencies of atoms, so the light beam experiences absorption phenomenon. In this case, the light beam will be attenuated as it progresses [38].

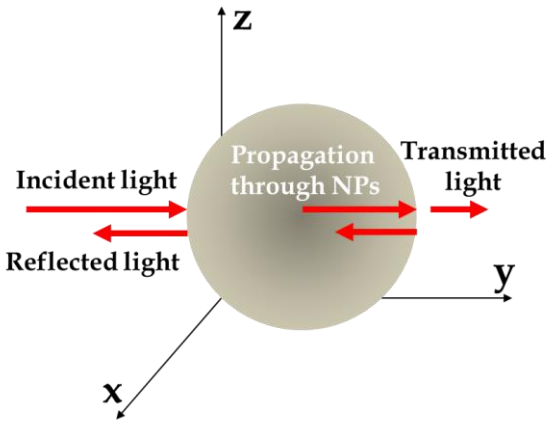

Figure 1. Illustration of the interaction between light and nanoparticle.

The absorption of light by nanoparticles can be quantified in terms of the absorbance (A). This is sometimes called the optical density (OD). Mathematically, the absorbance can be represented as follows [38],

$$A = -\log_{10}\left(\frac{I(l)}{I_o}\right) = 0.434al \tag{8}$$

where $I(l)$ is the intensity of light being propagated, I_o is the initial intensity of light, l is the path length, and a is the absorption coefficient. This coefficient is defined as the fraction of the power absorbed in the unit of length of the medium [38].

The propagation of a light beam through the nanoparticles depends on their refractive index. The refracted index of nanoparticles depends on the frequency of the light beam. This is called dispersion relation. Since, the refractive index can be represented mathematically by a complex number, such as

$$\tilde{n} = n + i\kappa \tag{9}$$

where n represents the real refractive index and κ represents the extinction coefficient. As mentioned, the extinction coefficient is associated with the absorption of a light beam by the nanoparticles so that the light beam decreases its amplitude. Therefore, the extinction coefficient is linearly proportional to the absorption coefficient [39], as follows

$$\kappa = \frac{a\lambda}{4\pi} \tag{10}$$

The refractive index $\tilde{n}$ has a mathematical relation to the dielectric constant $\tilde{\varepsilon}$. By using Maxwell's equations, it is very easy to derive the relation between those constants, as follows,

$$\tilde{n} = \sqrt{\tilde{\varepsilon}} \tag{11}$$

For n is complex than ε also complex, so that the dielectric constant will be [38],

$$\tilde{\varepsilon} = \varepsilon_r + i\varepsilon_i \tag{12}$$

According to (9), so the real and imaginary part of the dielectric constant can be calculated by using the following equations,

$$\varepsilon_r = n^2 - \kappa^2 \tag{13}$$

$$\varepsilon_i = 2n\kappa \tag{14}$$

The dissipation factor of the nanoparticles can be calculated by using those dielectric constants through the following equation [39],

$$\tan\delta = \frac{\varepsilon_i}{\varepsilon_r} \tag{15}$$

When the nanoparticles interacted with a photon, so the nanoparticles would perform their photoconductive property. The property can be quantified in terms of optical conductivity as follows [39],

$$\sigma_{opt} = \frac{anc}{4\pi} \tag{16}$$

where c represents the light velocity (3.0×10^8 m/s).

The optical properties of nanoparticles are strongly correlated with the symmetry of the lattice [40]. In case, optically isotropic crystalline nanoparticles, such as Fe_3O_4 has cubic symmetry. Therefore, the optical constants along all crystal directions have the same value. For instant, the refractive index and dielectric constant are not varied according to the vibration direction of the light beam. Accordingly, any type of lattice distortion or structural disorder can influent the optical properties of the nanoparticles, such as the formation of a localized state between the valence band and the conduction band. The energy associated with this state is well-known as Urbach energy (E_u). This energy is estimated toward a plot between $ln\ a$ (absorption coefficient) and photon energy $h\nu$ according to the following equation [39],

$$a = a_o \exp\left(h\nu / E_u\right) \tag{17}$$

where h is Planck's constant (6.67×10^{-34} Js) and ν is photon frequency (Hz).

Surface Plasmon Resonance Based Sensor:

Generally, the surface plasmon resonance-based sensor has the most popular metal-dielectric configurations on the ATR method, e.g., Otto and Kretschmann configurations. On the Kretschmann's configuration, the metal layer (e.g., gold and silver) with a premittivity constant $\tilde{\varepsilon}_m$ and thickness t is employed onto the prism's surface with a permittivity of $\tilde{\varepsilon}_p$ and refractive index $\tilde{n}_p$. Meanwhile, on the Otto's configuration, the metal layer must be separated from the prism's surface by using a spacer layer. For

multilayer structure, the metal surface can be coupled by dielectric-metal layer such as Fe_3O_4 nanoparticles with permittivity constant of $\tilde{\varepsilon}_d$ ($\tilde{\varepsilon}_d < \tilde{\varepsilon}_p$) [41].

In both configurations, the incident *p*-polarized light beam from the polarizer is shone to the prism's surface. This light beam is reflected at the interface between the prism's surface and the metal layer. The reflected light will be captured by the photodetector. During reflection, a part of the light beam will be reflected in the prism and a part is propagated in the metal in the form of an inhomogeneous wave called an evanescent wave (propagation constant of $\vec{k}_S$). This wave will penetrate through the metal and excite a surface plasmon wave (SPW – propagation constant of $\vec{k}_{SPW}$) on the interface between metal and a dielectric layer (the Fe_3O_4 layer). The SPW propagation constant can be calculated by the following equation,

$$\vec{k}_{SPW} = \vec{k}_o \sqrt{\frac{\tilde{\varepsilon}_m \tilde{\varepsilon}_d}{\tilde{\varepsilon}_m + \tilde{\varepsilon}_d}} \tag{18}$$

where $\vec{k}_o$ is the propagation constant of the incident light. The resonance occurs when the propagation constant of the evanescent wave is equal to the propagation constant of the SPW, as follows,

$$\vec{k}_o \tilde{n}_p \sin\theta_{SPR} = \vec{k}_o \sqrt{\frac{\tilde{\varepsilon}_m \tilde{\varepsilon}_d}{\tilde{\varepsilon}_m + \tilde{\varepsilon}_d}} \tag{19}$$

In terms of an effective index (see (11)), the resonance condition can be rewritten as follows,

$$\tilde{n}_p \sin\theta_{SPR} = \sqrt{\frac{\tilde{\varepsilon}_m \tilde{n}_d^2}{\tilde{\varepsilon}_m + \tilde{n}_d^2}} \tag{20}$$

Moreover, the resonance angle satisfies,

$$\theta_{SPR} = \sin^{-1}\left(\frac{1}{n_p} \sqrt{\frac{\tilde{\varepsilon}_m \tilde{n}_d^2}{\tilde{\varepsilon}_m + \tilde{n}_d^2}} \right) \tag{21}$$

for $\tilde{n}_p = n_p$ [41]. The resonance angle (SPR-angle) depends on the refractive index of the dielectric layer.

Experimental Method

Materials and Reagents:

The main material used to prepare the Fe_3O_4 samples was iron sand. Iron sand was taken from Wari Ino Beach Halmahera Utara. This material is the source for supplying Fe element. In another hand, the reagents e.g., HCl (Sigma Aldrich) and NaOH (Sigma Aldrich) were used as oxydator and co-precipitator. Distilled water was used as a solvent for the chemical synthesis.

Preparation of the Fe_3O_4 Samples:

The Fe_3O_4 nanoparticles were prepared using the chemical coprecipitation method. Systematically, a complete procedure has been depicted in Figure 2. There are two stages to this preparation. First, preparation of $FeCl_3$ and $FeCl_2$ solutions. As mentioned, the iron sand was the source for the Fe element. Iron sand of 2 grams was dissolved in 20 mL HCl

(37%) at room temperature while stirred at a constant rate of 500 rpm for 10 minutes. A high mixing rate was purposed to effectively extract the Fe element and react with HCl to provide $FeCl_3$ and $FeCl_2$ solutions. Both $FeCl_3$ and $FeCl_2$ would be produced simultaneously (called a FeCl solution). This solution has a strong yellow color. The solution of 20 ml was separated from the rough sand by using Whatman filter paper.

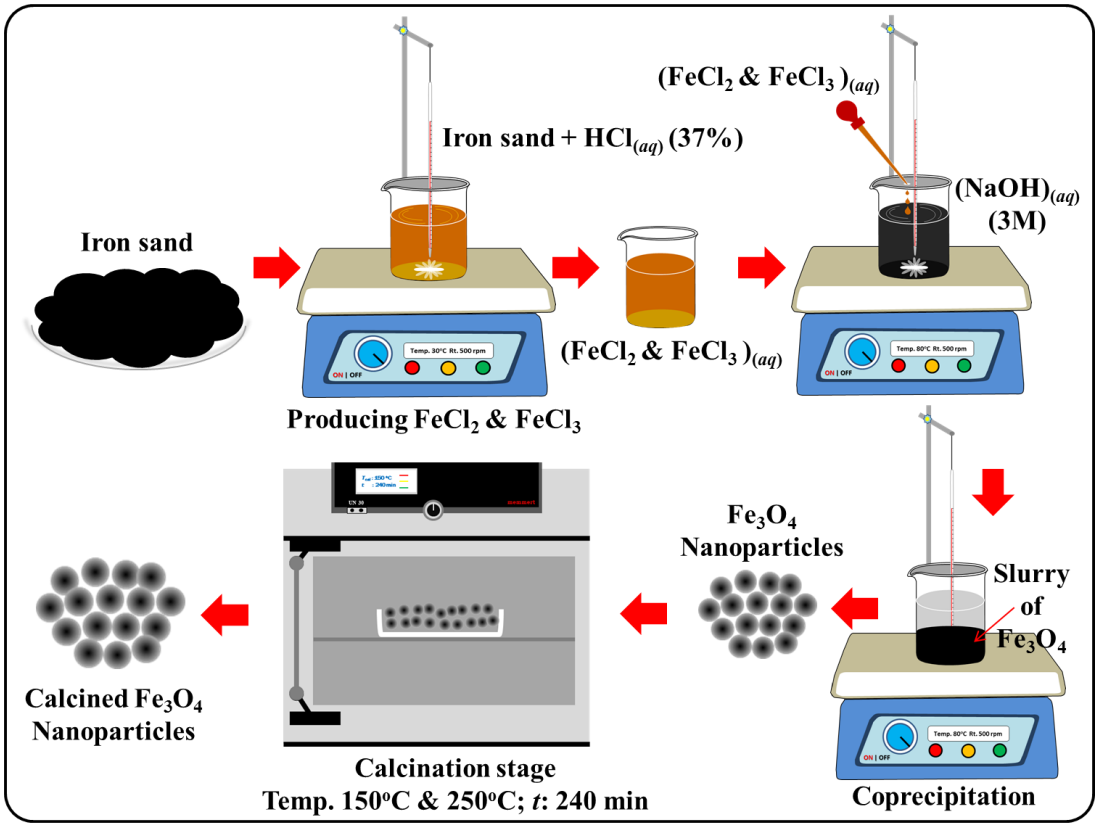

Figure 2. Ilustration of the preparation procedure for Fe_3O_4 nanoparticles.

Second, the preparation of Fe_3O_4 powder. The NaOH solution of 3M was prepared. The solution was stirred at a constant rate of 500 rpm while heated up to the temperature of 80°C. This temperature was maintained constantly.

After the temperature was 80°C, the FeCl solution was dropped constantly into the NaOH solution. Make sure that the process was conducted in an isolated system (the beaker was closed up, only a small hole available for the pipette). After dropping, the hole was closed. The solution was stirred at this temperature for about 60 minutes since the first dropping. After the coprecipitation stage finished, the temperature was lowered to 30°C. Please, wait for the solution to experienced thermal equilibrium at this temperature. The slurry of nanoparticles will be separated with the solvent due to magnetic and gravitational forces. The slurry was rinsed five times by using distilled water. The slurry was filtered and heated up to the temperature of 100°C in the oven. The heating process was conducted for 4 hours at that constant temperature. This process provided black chips of Fe_3O_4. These chips were ground to produce a smooth powder of Fe_3O_4 nanoparticles. Finally, the powder of Fe_3O_4 nanoparticles was calcined in an oven at temperatures of 150°C and 250°C for 4 hours.

Characterization of the Fe_3O_4 Samples:

The prepared powder of Fe_3O_4 nanoparticles was characterized by powder X-ray diffraction (XRD) and Specular Reflectance UV-Visible spectroscopy techniques. The diffraction patterns of samples were recorded by using PanAnalytical-Expert Pro X-ray diffractometer equipped CuKα anode ($\lambda_{Cu\text{-}K\alpha}$ = 1.5405980 Å) with a scan step size of 0.02°. The absorbance spectra of samples were recorded by using Pharmaspec UV-Vis 1700 series spectrophotometer with a scan step size of the wavelength of 1 nm.

Result and Discussion

X-Ray Diffraction Patterns and the Structural Properties:

The diffraction patterns of Fe_3O_4 are depicted in Figure 3a. The patterns show that the Fe_3O_4 nanoparticles are polycrystalline materials in nature. They are indicated by the appearance of diffractions peaks belong to their reflection planes such as (220), (311), (440), (422), (511), (440), and (533). Those diffraction peaks are valid to the reference available in JCPDS card no. 11-0614 for the Fe_3O_4 phase with a cubic spinel structure. In particular, there is an extra peak appear on the diffraction pattern of the sample calcined at a temperature of 150°C. That peak is a diffraction peak of the Fe_2O_3 in the maghemite phase with the reflection plane of (115) according to JCPDS card no. 11-0615.

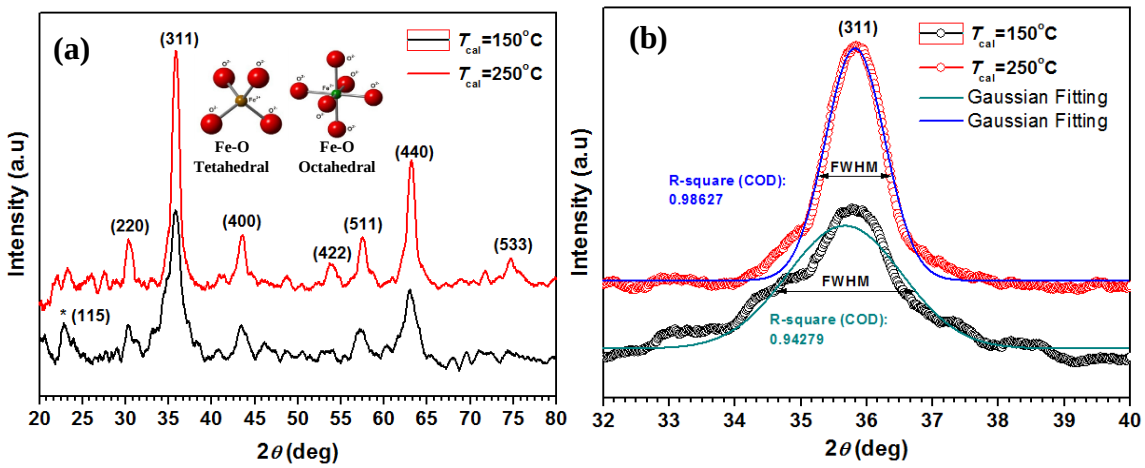

Figure 3. (a) Diffraction patterns of Fe_3O_4 nanoparticles and (b) Gaussian fitting for peak of (311). The geometrical structures of the Fe-O tetrahedral and Fe-O octahedral coordination are displayed in (a).

These patterns show that diffraction of X-ray by the reflection plane of (311) has the highest intensity. It implies that the most number of crystallite in the samples ordered along the lattice direction of (311). The peaks are also sharp which indicates that the formation of larger crystallites. However, the diffraction peaks of Fe_3O_4 (250°C) are sharper than Fe_3O_4 (150°C). This is shown in Figure 3b. The FWHM of its peak (especially for (311)) is smaller. In another hand, more noise is the appearance of the diffraction pattern of Fe_3O_4 (150°C). In short, Fe_3O_4 (250°C) has a higher degree of crystallinity than Fe_3O_4(150°C).

As mentioned, the particle size of Fe_3O_4(250°C) is larger than Fe_3O_4(150°C). By using the Williamson-Hall method, plot sin θ_{hkl} (x-axis) versus β_{hkl} cos θ_{hkl} (y-axis) can be depicted in

Figure 4. According to the plots, the calculated particle size is 5.39 nm and 15.96 nm, consecutively for Fe_3O_4(150°C) and Fe_3O_4(250°C) (Table 2). Higher calcination temperature can improve the crystallinity and particle size of the nanoparticles. Their physical mechanism can be explained as follow. Calcination facilitates the nanoparticles to experience renucleation and recrystallization process due to a higher thermal energy supply. Some small nuclei will be joined to produce larger nuclei. Some nucleis might be growing larger by themself. The formation of new nuclei is followed by a densification process in which the nanoparticles became denser. The nanoparticles became more regular [29].

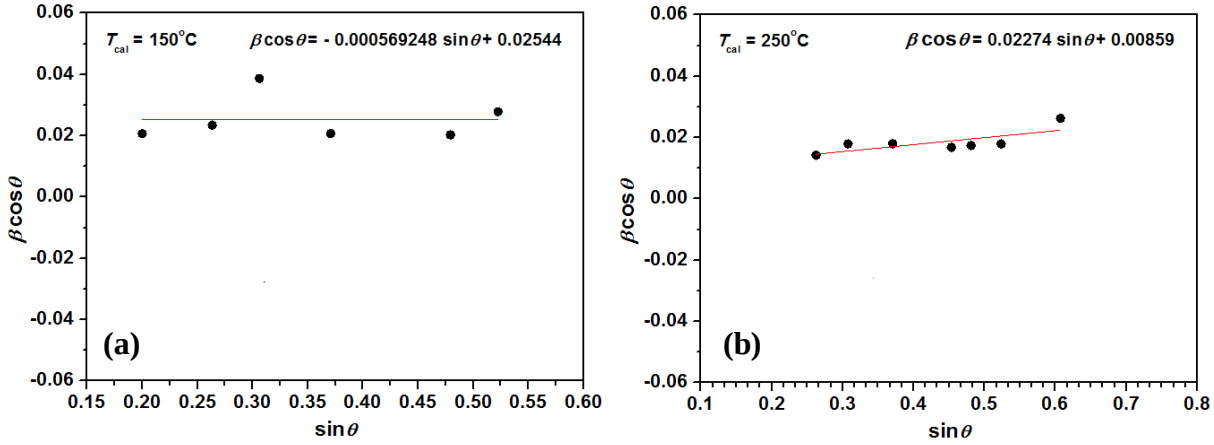

Figure 4. The Williamson-Hall plots: (a) Fe_3O_4 (150°C) and (b) Fe_3O_4 (250°C).

Table 2. Structural parameters of Fe_3O_4 nanoparticles.

Cal. Temp. (°C)	t (nm)	$a_{(311)}$ (Å)	ε (× 10^{-4})
150	5.39	8.3665	- 1.42
250	15.96	8.3276	56.86

Another effect on the difference in calcination temperature is a change in the lattice parameter. The Fe_3O_4 (150°C) has a longer lattice parameter than Fe_3O_4 (250°C). The thermal energy given during calcination will cause a shrinkage on the lattice parameter. Due to a thermal energy diffusion in the nanoparticles, so that the atoms in the edge of the unit cell change their position. During calcination, the position among atoms becomes closer as higher thermal energy is absorbed by the nanoparticle. Atomic dislocation produces crystal imperfection such as point defect. Those crystal imperfections produce intrinsic strain in the lattice. The strain is typically uniform and isotropic. Since this strain will cause a broadening of the diffraction peaks. Numerically, the lattice strain of Fe_3O_4 (150°C) is negative. It might imply that the existence of compressive strain on the lattice of the nanoparticles [33].

Optical Properties:

Absorption is one of the phenomena that occurs when an electromagnetic wave interacts with a material. The absorption of light by the material can be quantified in the form of a physical quantity known as absorbance. The absorbance spectra of the Fe_3O_4 nanoparticles can be depicted in Figure 5a. However, according to (8), the ability of the Fe_3O_4 to absorb light energy can be associated with the absorption coefficient. The associated absorption coefficient versus light energy can be depicted in Figure 5b.

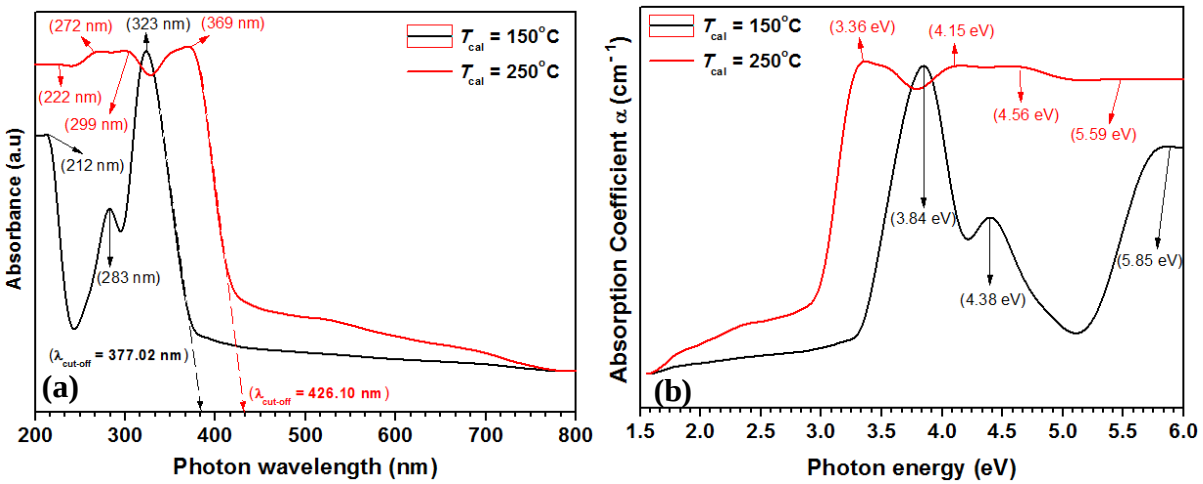

Figure 5. (a) Absorbance spectra and (b) absorption coefficient of the Fe_3O_4 nanoparticles.

According to Figure 5a., there are three absorption peaks investigated in the absorbance spectra of the Fe_3O_4(150°C). However, there are four peaks in the Fe_3O_4 (250°C). Those peaks represent the absorption of light with the associated wavelength and energy by electrons for conducting interband transitions. The most interesting of these findings that the highest absorbance peak of the Fe_3O_4 (250°C) occurs at a higher photon wavelength than Fe_3O_4 (150°C). This implies the largest energy needed by electrons of the Fe_3O_4 (150°C) to conduct interband transition is higher than Fe_3O_4 (150°C), as shown in Figure 5b. Accordingly, the distance between two bands in the electronic structure of the Fe_3O_4 (250°C) is shorter than Fe_3O_4 (150°C). Furthermore, the cut-off wavelength of the Fe_3O_4 (250°C) is higher than the Fe_3O_4 (150°C). It informs that the optical gap energy between the lowest unoccupied conduction band and the highest occupied valence band of the Fe_3O_4 (250°C) is smaller than Fe_3O_4 (150°C). These findings agree with the results reported by [29].

The particle size has a significance to influence the optical properties of the nanoparticles. In this case, the optical gap energy is strongly affected by its particle size. As a quantum confinement effect, larger particle size will give a smaller optical gap energy, smaller gap between the conduction band and the valence band, as reported by [42–44]. In another hand, lattice strain also significantly affects the absorbance of the nanoparticles. Accordingly, the appearance of regions with a weak absorbance in the absorbance spectra of the Fe_3O_4 (250°C) might be caused by the lattice strain. Lattice deformation and the displacement of the atomic position cause a change in the electronic band structure. Moreover, chemical defects and impurity due to higher calcination temperature also influence the absorbance of the nanoparticles [44].

The refractive index and the extinction coefficient of Fe_3O_4 nanoparticles can be depicted in Figure 6. The refractive index is associated with the degree of transparency of the material. The refractive index reveals how fast light travels through the nanoparticles. Accordingly, the refractive index of the Fe_3O_4 varies with photon wavelength. Due to the absorption of light, so that the refractive index has to be represented with a complex number. The real part

accounts for refraction, while the imaginary part represents the attenuation of light intensity due to absorption. The imaginary part is associated with the extinction coefficient.

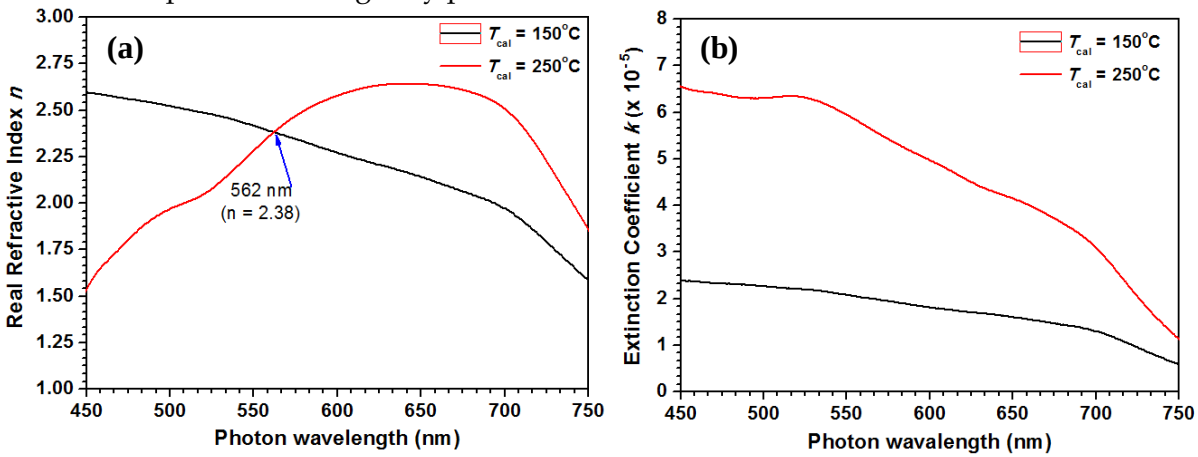

Figure 6. (a) Refractive index and (b) extinction coefficient of the Fe_3O_4 nanoparticles.

According to Figure 8a., the critical refractive index of the Fe_3O_4 occurs at a wavelength of 562 nm (n = 2.38). At this point, the refractive index of those samples is the same. At a larger wavelength, the refractive index of the Fe_3O_4 (250°C) goes larger than Fe_3O_4 (150°). In another hand, a higher attenuation of light consistently occurs in the Fe_3O_4 (250°C) for all wavelength values. Specifically, the complex refractive index of the Fe_3O_4 at a wavelength of 632.8 nm is provided in Table 3. These values are in agreement with the results reported by [26,45]. In short, the lattice strain and particle size also influence the refractive index of the nanoparticles.

Table 3. The refractive index and dielectric constant of Fe_3O_4 nanoparticles.

Calcination Temp.	t (nm)	n	k	ε_r	ε_i
150 °C	5.39	2.187	1.683×10^{-5}	4.787	7.364×10^{-5}
250 °C	15.96	2.642	4.376×10^{-5}	6.979	23.120×10^{-5}

According to (13) and (14), the refractive index has a relation to the dielectric constant of the nanoparticles. The dielectric constant of the Fe_3O_4 can be depicted in Figure 7. Systematically, the dielectric constant has a the same trend as the refractive index. The value of the dielectric constant can be described by using a complex number. Both real and imaginary parts of dielectric constant for Fe_3O_4 (250°C) are larger than Fe_3O_4 (150°C). At a critical wavelength of 562 nm, their real part of the dielectric constant is 5.67. A change in the dielectric constant within the range of the photon wavelength can be attributed to a change in the polarization due to valence states of cations Fe^{2+} and Fe^{3+}; and space charges polarization. From the crystal point of view, this phenomenon can be explained as follows. The Fe^{2+} and Fe^{3+} cations can make a dipole of $Fe^{2+} \leftrightarrow Fe^{3+}$. This dipole can change to be $Fe^{3+} \leftrightarrow Fe^{2+}$ at a lower wavelength of the photon. There happen an electronic hopping between Fe^{2+} and Fe^{3+}. This hopping influences the polarization of those dipoles and finally the dielectric constant of the nanoparticles. Clearly, in this case, the lattice strain and defect strongly determine the formation of those dipoles and their polarization.

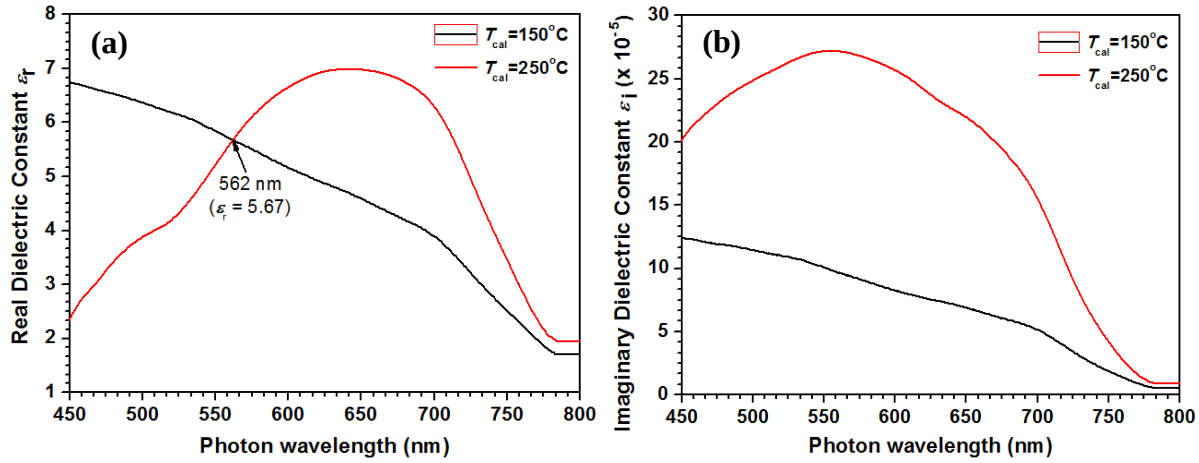

Figure 7. (a) Real part and (b) imaginary part of the dielectric constant of Fe_3O_4 nanoparticles.

As shown by (15), the dissipation factor of the nanoparticles over photon energies can be depicted in Figure 8a. The dissipation factor increases as the energy increases. This implies that increasing photon energy will cause more energy released as heat by the nanoparticles [39]. Lattice defect and vacancies also contribute to the amount of energy released as heat toward the dipole formation and their polarization.

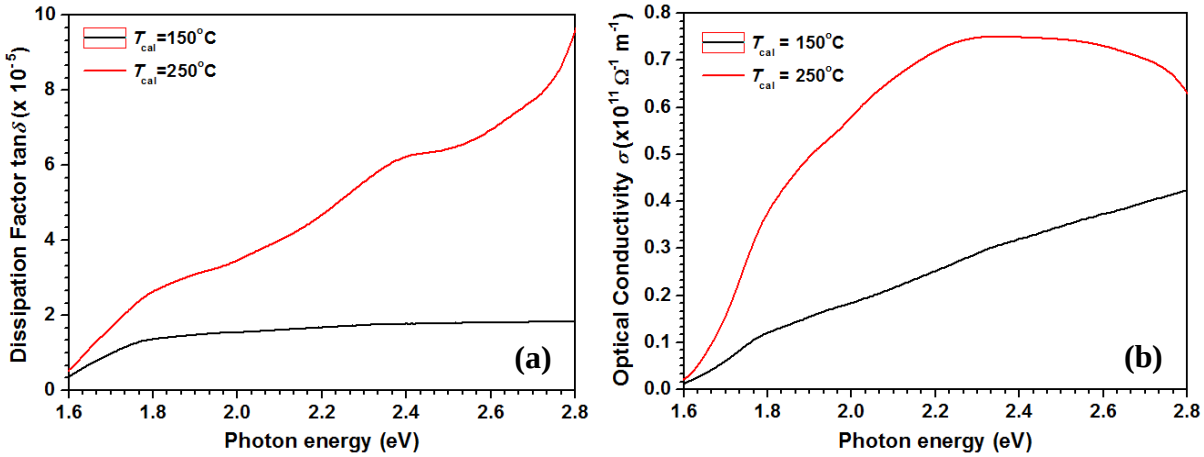

Figure 8. (a) Dissipation factor and (b) optical conductivity of Fe_3O_4 nanoparticles.

According to Figure 10b., the optical conductivity of the Fe_3O_4 increases as photon energy increasing in a region of 1.6 eV – 2.8 eV. This finding coincides with the result reported by [26]. In these energy regions, the optical conductivity of the Fe_3O_4 (250°C) is larger than Fe_3O_4 (150°C). This means that the optical excitation of the electrons without the presence of an applied electric field within the Fe_3O_4 (250°C) occurs more massive compared to Fe_3O_4 (150°C). In another hand, this might be due to a larger concentration of the charge carrier appear within the Fe_3O_4 (250°C).

The appearance of lattice strain due to chemical defect and vacancy in a crystalline material influences the electronic structure of the material, such as the Fe_3O_4 nanoparticles. Lattice strain probably affects the formation of additional states between the conduction band and

the valence band. This states like a band tail for those two bands. The energy between those band tails is represented in form of Urbach energy, as shown by (17). The Urbach energy of the Fe_3O_4 can be depicted in Figure 9.

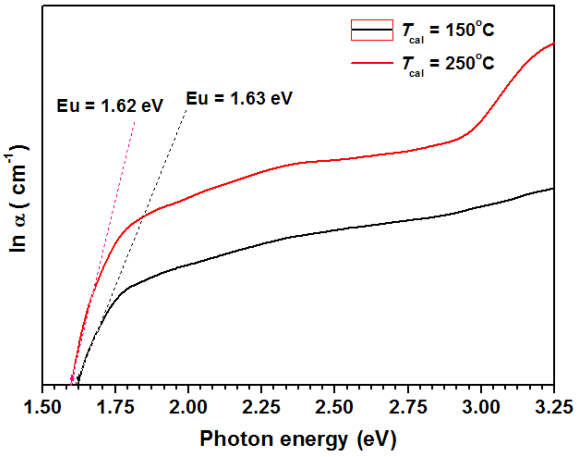

Figure 9. Urbach energy of Fe_3O_4 nanoparticles.

Lattice strain and the particle size attribute the Urbach energy of the nanoparticles. As shown, the Urbach energy of the Fe_3O_4 (250°C) is smaller than Fe_3O_4 (150°C). This can be explained as follows. First, as explained that larger particle size will produce smaller optical gap energy due to the quantum confinement effect. The Fe_3O_4 (250°C) has smaller optical gap energy therefore it has smaller Urbach energy. Notice that the Urbach energy is measured as a gap between the band tails below the conduction band and upper the valence band, as illustrated by [46]. Second, larger lattice strain doesn't mainly affect the values of the Urbach energy. A material with a smaller particle size and larger lattice strain will produce larger Urbach energy.

SPR-Based Sensor Simulation:

Simulation of the SPR phenomena was carried out using *Winspall version 3.02 plasmon simulator software*. The simulation parameters are listed in Table 4. First of all, the reflection curve of prism BK7 has been recorded with an incident angle range of 10° – 70°. This curve is depicted in Figure 10a. The total internal reflection (TIR) phenomenon was investigated at a critical angle of 41.67°. At this point, about 92% of the incident light experienced the TIR phenomenon as it was set under *p*-polarization mode. The SPR angle was expected to be above 41.67° because below this angle the SPR phenomenon can't occur due to insufficient energy supplied by the light beam. Furthermore, the reflectivity of this curve falls to near zero at an incident angle of 33.52°. The reflectivity is about 4.88×10^{-9}. This incident angle is a Brewster angle, which indicates the existence of the SPR phenomenon (Figure 10b). Brewster angle is very crucial since *p*-polarization mode can generate the surface plasmon [47].

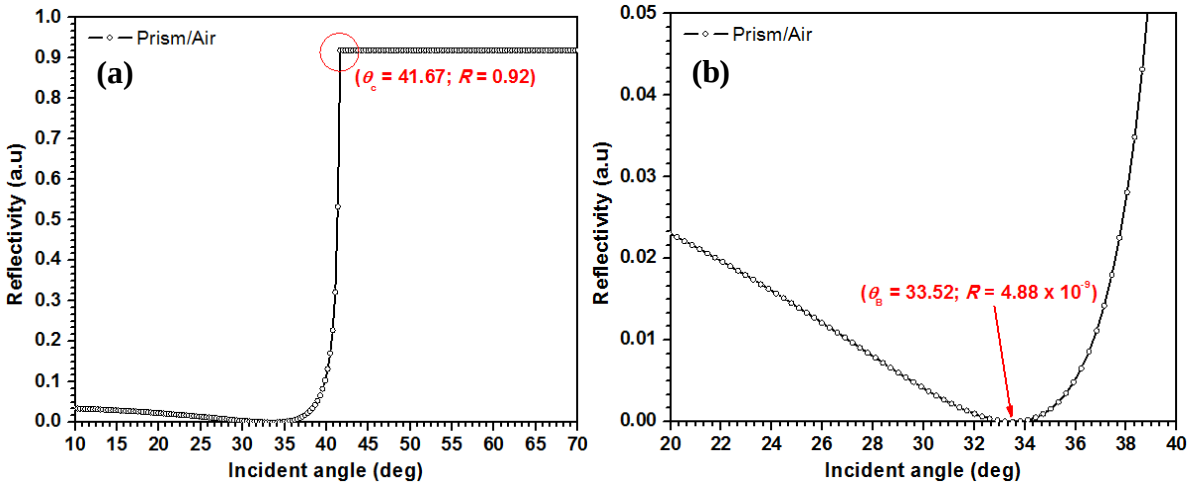

Figure 10. (a) Critical angle for TIR phenomenon and (b) the Brewster angle.

Table 4. Simulation parameters for SPR-based sensor.

Layer	***t* (nm)**	n_{real}	***k***
Prims	-	1.51	-
Au	50	0.1838	3.4313
Fe_3O_4 (150)	5.39	2.1879	1.6830×10^{-5}
Fe_3O_4 (250)	15.96	2.6418	4.3757×10^{-5}
Air	-	1	-

According to Table 3., in this simulation, we have three systems, e.g., Prims/Au/Air; Prims/Au/Fe_3O_4 (150°C)/Air; and Prism/Au/Fe_3O_4 (250°C)/Air (Table 5). The reflectance curve for Prims/Au/Air system can be depicted in Figure 11a. Here, a strong signal of about 85.9% of the light energy was used to excite the surface plasmon wave under the *p*-polarized light beam. The sensor showed a positive response of about 2.8% at an incident angle of 44.07°. By using Lorentz fitting, so the FWHM value of the reflectance curve (dip) for this system is about 0.98° ± 0.05°.

The addition of the Fe_3O_4 (150°C) and Fe_3O_4 (250°C) on the gold layer influences the response of the SPR-sensor. As provided in Table 3., the thickness of the Fe_3O_4 layer was assumed approach to their particle size. It means there only one layer nanoparticles deposited on the gold layer. In short, this was conducted for a reason to investigate the effect of the Fe_3O_4 particles size on the SPR-sensor response. According to Figure 11b., for an addition of the Fe_3O_4 (150°C), about 85.94% of the incident light was excited as a surface plasmon wave. Meanwhile, about 85.69% of the incident light was excited as a surface plasmon wave for an addition of the Fe_3O_4 (250°C). The FWHM of the reflectance curve for the Fe_3O_4 (250°C) is larger than Fe_3O_4 (150°).

The excitation of the surface plasmon wave occurred at an incident angle of 42.56° and 44.67°, consecutively for the Fe_3O_4 (150°C) and Fe_3O_4 (250°C). The resonance between the surface plasmon wave and the evanescent wave occurred at an incident angle of 45.28° and 54.02°, consecutively for the Fe_3O_4 (150°C) and Fe_3O_4 (250°C). The associated reflectivity for those

resonance angles is 0.006 and 0.004. It shows that the SPR-angle shifting. There is only 0.4% of the incident light energy reflected when the resonance occurred in the system of Prism/Au/Fe_3O_4 (250°C)/Air. It is smaller compared with the system of Prism/Au/Fe_3O_4 (150°C)/Air. The FWHM value was increased from 1.34° ± 0.08° to 5.53° ± 0.43°.

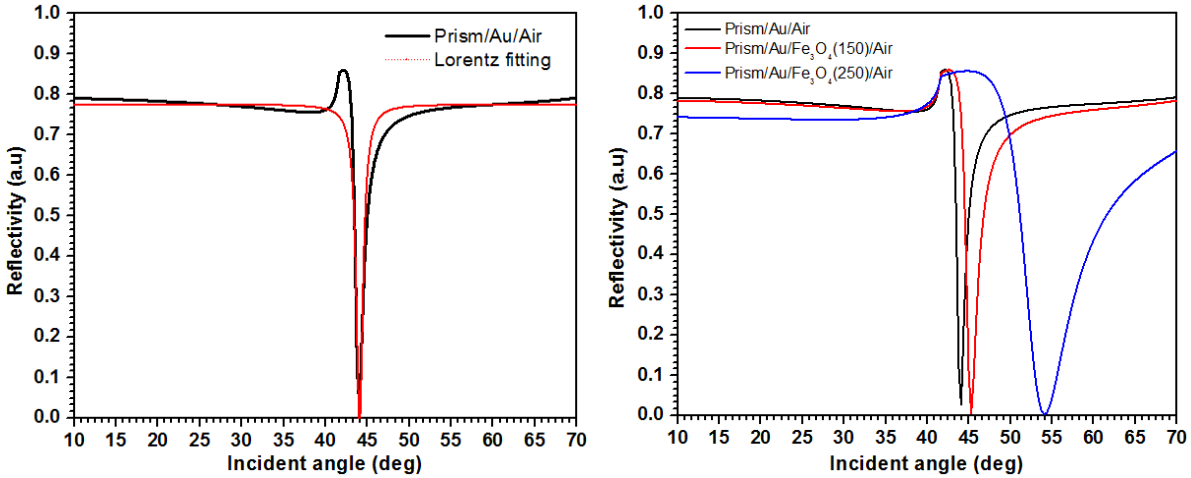

Figure 11. (a) SPR-curve of Prism/Au/Air system and (b) SPR-curves for systems of Prims/Au/Fe_3O_4 (150°)/Air and Prims/Au/Fe_3O_4(250°C)/Air.

Table 5. SPR-angles, reflectivity, and the FWHM of the reflection curve.

System	θ_{SPR} (°)	*R* (a.u)	FWHM (°)
Prims/Au/Air	44.07	0.028	0.98 ± 0.05
Prism/Au/Fe_3O_4(150)/Air	45.28	0.006	1.34 ± 0.08
Prism/Au/Fe_3O_4(250)/Air	54.02	0.004	5.53 ± 0.43

Those phenomena can be explained as follows. First, shifting the SPR-angle to a larger value is attributed to an increase of the refractive index of the Fe_3O_4. As provided in Table 3, the refractive index of the Fe_3O_4 (250°C) is larger than Fe_3O_4 (150°C). It justifies that by enhancing the refractive index of the system, so the SPR-sensor signal becomes stronger.

The refractive index of the system can be used to amplify the SPR-signal. Second, the larger width (FWHM) of the resonance curve for Prism/Au/Fe_3O_4 (250°C)/Air compared to Prism/Au/Fe_3O_4 (150°C)/Air is attributed to the complex value of the metal's dielectric constant. The complex dielectric constant of Fe_3O_4 (250°C) is larger than Fe_3O_4 (150°C). Mainly, a larger imaginary part of the dielectric constant will produce a larger FWHM of the resonance curve. Moreover, the real part of the dielectric constant determines the position of the SPR-angle. It is a consequence of (13).

Conclusion

This research has been investigated the effect of particle size and lattice strain on the optical properties of the Fe_3O_4 nanoparticle and their potential application in SPR-sensor. The particle size of the nanoparticle has been successfully controlled by using calcination temperatures of 150°C and 250°C. Major results of this work show that larger particle size implicate to a larger refractive index and complex dielectric constant, but smaller optical gap

energy and the Urbach energy of the Fe_3O_4. However, the lattice strain due to chemical defect and vacancy directly affect the band structure of the nanoparticles which implicates all optical parameters. Furthermore, a simulation of SPR-sensor has been successfully carried out. The most interesting findings show that the optical properties of the Fe_3O_4 strongly affect the SPR phenomena.

The Fe_3O_4 nanoparticle with a larger refractive index and real part of the dielectric constant will produce a larger SPR-angle shift. The imaginary part of the dielectric constant contributes to the resonance curve width. In short, controlling the particle size and minimizing the lattice strain of the Fe_3O_4 will allow us to boost their performance as a signal amplifier in the SPR-sensor. Future works are available for investigating the particle size, lattice strain, and the optical properties of the Fe_3O_4 by using advanced characterization techniques for providing deeper scientific facts.

Acknowledgment

The authors would like thank to Kemenristek-Dikti for full financial support toward PDP Research Grant year 2019-2020 with a contract number of 337/LL12/KM/2020. An acknowledgment would also deliver to LPPMP Universitas Halmahera for the administration services of this grant.

References

[1] Ahmadi S, Chia C H, Zakaria S, Saeedfar K & Asim N (2012). Synthesis of Fe_3O_4 Nanocrystals using Hydrothermal Approach. *J. Magn. Magn. Mater.*, 324, 4147–50.

[2] Montoro V (1938). Miscibilita Fra Gli Ossidi Salini di Ferro e di Manganese. *Gazz. Chim. Ital.*, 68, 728–33.

[3] Dukenbayev K, Korolkov I V, Tishkevich D I, Kozlovskiy A L, Trukhanov S V, Gorin Y G, Shumskaya E E, Kaniukov E Y, Vinnik D A, Zdorovets M V, Anisovich M, Trukhanov A V, Tosi D & Molardi C (2019). Fe_3O_4 Nanoparticles for Complex Targeted Delivery and Boron Neutron Capture Therapy. *Nanomaterials*, 9, 1–19.

[4] Sirivat A & Paradee N (2019). Facile Synthesis of Gelatin-Coated Fe_3O_4 Nanoparticle: Effect of pH in Single-Step Co-precipitation for Cancer Drug Loading. *Mater. Des.*, 181, 107942.

[5] Anwar S, Khawja M, Ficiar E, Ruffinatti F A, Stura I, Argenziano M, Abollino O, Cavalli R, Guiot C & Agata F D (2019). Magnetic Iron Oxide Nanoparticles: Synthesis, Characterization and Functionalization for Biomedical Applications in the Central Nervous System. *Materials (Basel).*, 12, 1–24.

[6] Bruschi M L & Toledo L A S (2019). Pharmaceutical Applications of Iron-Oxide Magnetic Nanoparticles. *Magnetochemistry*, 5, 1–19.

[7] Nazri N A A, Azis S R, Man H C, Ismail I & Ibrahim I R (2019). Extraction of Magnetite from Millscales Waste for Ultrafast Removal of Cadmium Ions. *International J. Eng. Adv. Technol.*, 9(1), 5902–5907.

[8] Sureshkumar V, Daniel S C G K, Ruckmani K & Sivakumar M (2016). Fabrication of Chitosan – Magnetite Nanocomposite Strip for Chromium Removal. *Appl. Nanosci.*, 6, 277–285.

[9] El-khawaga A M, Farrag A A, Elsayed M A, El-Sayyad G S & El-Batal A I (2020).

Antimicrobial and Photocatalytic Degradation Activities of Chitosan-coated Magnetite Nanocomposite. *J. Clust. Sci.*, 6, 1–13.

[10] Feng A, Jia Z, Zhao Y & Lv H (2018). Development of Fe/Fe_3O_4@C Composite with Excellent Electromagnetic Absorption Performance. *J. Alloys Compd.*, 745, 547–554.

[11] Zeng Z, Zhao H, Wang J, Lv P, Zhang T & Xia Q (2014). Nanostructured Fe_3O_4@C as Anode Material for Lithium-ion Batteries. *J. Power Sources*, 248, 15–21.

[12] Suhanto R N, Harimurti S, Septiani N L W, Utari L, Anshori I, Wasisto H S, Suyatman, Suzuki H & Yuliarto B (2020). Sonochemical Synthesis of Magnetic - Fe_3O_4/Graphene Nanocomposites for Label-Free Electrochemical Biosensors. *J. Mater. Sci. Mater. Electron.*, 1–13.

[13] Thu N T A, Duc H V, Phong N H, Cuong N D, Hoan N T V & Khieu D Q (2018). Electrochemical Determination of Paracetamol Using Fe_3O_4/Reduced Graphene-Oxide-Based Electrode. *J. Nanomater.*, 1–15.

[14] Satvekar R K, Rohiwal S S, Tiwari A P, Raut A V, Tiwale B M & Pawar S H (2015). Sol – gel Derived Silica/Chitosan/Fe_3O_4 Nanocomposite for Direct Electrochemistry and Hydrogen Peroxide Biosensing. *Mater. Res. Express.*, 2, 1–10.

[15] Zhang W, Li X, Zou R, Wu H, Shi H, Yu S & Liu Y (2015). Multifunctional Glucose Biosensors from Fe_3O_4 Nanoparticles Modified Chitosan/Graphene Nanocomposites. *Sci. Rep.*, 5, 1–9.

[16] Saif S, Tahir A & Chen Y (2016). Green Synthesis of Iron Nanoparticles and Their Environmental Applications and Implications. *Nanomaterials*, 6, 1–26.

[17] Ghazanfari M R, Kashefi M, Shams S F & Jaafari M R (2016). Perspective of Fe_3O_4 Nanoparticles Role in Biomedical Applications. *Biochem. Res. Int.*, 1–32.

[18] Gao G, Shi R, Qin W, Shi Y, Xu G, Qiu G & Liu X (2010). Solvothermal Synthesis and Characterization of Size-Controlled Monodisperse Fe_3O_4 Nanoparticles. *J. Mater. Sci.*, 45, 3483–3489.

[19] Manikandan A, Vijaya J J, Mary J A, Kennedy L J & Dinesh A (2014). Structural, Optical and Magnetic Properties of Fe_3O_4 Nanoparticles Prepared by a Facile Microwave Combustion Method. *J. Ind. Eng. Chem.*, 20, 2077–2085.

[20] Kalantari K, Ahmed M B, Shameli K & Khandanlou R (2013). Synthesis of Talc/Fe_3O_4 Magnetic Nanocomposites using Chemical Co-precipitation Method. *Int. J. Nanomedicine*, 8, 1817–1823.

[21] Wu S, Sun A, Zhai F, Wang J, Xu W, Zhang Q & Volinsky A A (2011). Fe_3O_4 Magnetic Nanoparticles Synthesis from Tailings by Ultrasonic Chemical Co-precipitation. *Mater. Lett.*, 65, 1882–1884.

[22] Carvalho M D, Henriques F, Ferreira L P, Godinho M & Cruz M M (2013). Iron Oxide Nanoparticles: the Influence of Synthesis Method and Size on Composition and Magnetic Properties. *J. Solid State Chem.*, 201, 144–152.

[23] Rahman O, Mohapatra S C & Ahmad S (2012). Fe_3O_4 Inverse Spinal Superparamagnetic Nanoparticles. *Mater. Chem. Phys.*, 132, 196–202.

[24] Widanarto W, Sahar M R, Ghoshal S K, Arifin R, Rohani M S & Hamzah K (2013). Effect of Natural Fe_3O_4 Nanoparticles on Structural and Optical Properties of Er^{3+} Doped Tellurite Glass. *J. Magn. Magn. Mater.*, 326, 123–128.

[25] Rani S & Varma G D (2015). Superparamagnetism and Metamagnetic Transition in Fe_3O_4 Nanoparticles Synthesized via Co-precipitation Method at Different pH. *Phys. B Phys. Condens. Matter.*, 472, 66–77..

[26] Abd A N, Latif D M A & Abdulridha W M (2016). Synthesis and Some Physical

Properties of Magnetite (Fe_3O_4) NPs. *J. Multidiscip. Eng. Sci. Stud.*, 2, 341–345.

[27] Radoń A, Drygała A, Hawełek Ł & Łukowiec D (2017). Structure and Optical Properties of Fe_3O_4 Nanoparticles Synthesized by Co-precipitation Method with Different Organic Modifiers. *Mater. Charact.*

[28] Zulfiqar, Afzal S, Khan R, Zeb T, Rahman M, Burhanullah, Ali S, Khan G, Rahman Z & Hussain A (2018). Structural, Optical, Dielectric and Magnetic Properties of PVP Coated Magnetite - (Fe_3O_4) Nanoparticles. *J. Mater. Sci. Mater. Electron.*

[29] Indrayana I P T, Tjuana L A, Tuny M T & Kurnia (2019). Nanostructure and Optical Properties of Fe_3O_4: Effect of Calcination Temperature and Dwelling Time. *Journal of Physics Conference Series* (IOP Publishing), pp 1–10.

[30] Petrov D A, Ivantsov R D, Zharkov S M, Velikanov D A, Molokeev M S, Lin C, Tso C, Hsu H, Tseng Y, Lin E & Edelman I S (2020). Magnetic and Magneto-optical Properties of Fe_3O_4 Nanoparticles Modified with Ag. *J. Magn. Magn. Mater.*, 493, 1–10.

[31] Horia F, Easawi K, Khalil R, Abdallah S, El-mansy M & Negm S (2020). Optical and Thermophysical Characterization of Fe_3O_4 Nanoparticle *IOP Conf. Series: Materials Science and Engineering*, pp 2–10.

[32] Irfan H, Racik K M & Anand S (2018). Microstructural Evaluation of $CoAl_2O_4$ Nanoparticles by Williamson–Hall and Size–Strain Plot Methods. *J. Asian Ceram. Soc.*, 1–9.

[33] Rabiei M, Palevicius A, Monshi A, Nasiri S, Vilkauskas A & Janusas G (2020). Comparing Methods for Calculating Nano Crystal Size of Natural Hydroxyapatite Using X-Ray Diffraction. *Nanomaterials*, 10, 1–20.

[34] Augustin M & Balu T (2016). Estimation of Lattice Stress and Strain in Zinc and Manganese Ferrite Nanoparticles by Williamson–Hall and Size-Strain Plot Methods. *Int. J. Nanosci.*, 15, 1–7.

[35] El-Sadek M S A, Wasly H S & Batoo K M (2019). X‑ray Peak Profile Analysis and Optical Properties of CdS Nanoparticles Synthesized via the Hydrothermal Method. *Appl. Phys. A*, 125, 1–17.

[36] Chenari H M, Moafi H F & Rezaee O (2016). A Study on the Microstructural Parameters of $Zn_{(1-x)}La_xZr_xO$ Nanopowders by X-ray Line Broadening Analysis. *Mater. Res.*, 19, 548–554.

[37] Kaur P, Rahul, Kaur S, Kriti, Arora D, Asokan K & Singh D P (2019). Correlation Between Lattice Deformations and Optical Properties of Ni Doped ZnO at Dilute Concentration. *Mater. Today Proc.*, 1–6.

[38] Fox M. (2001). Optical Properties of Solids. Great Britain: Oxford University Press.

[39] Gherbi R, Bessekhouad Y & Trari M (2015). Structure, Optical and Transport Properties of Mg-Doped $ZnMn_2O_4$. *J. Alloys Compd.*, 655, 188–197.

[40] Weber M. J. (2003). Handbook of Optical Materials. United State of America: CRC Press LLC.

[41] Costa E B, Rodrigues E P & Pereira H A (2019). Sim-SPR : an Open-Source Surface Plasmon Resonance Simulator for Academic and Industrial Purposes. *Plasmonics*, 1–11.

[42] Loganathan A & Kumar K (2016). Effects on Structural, Optical, and Magnetic Properties of Pure and Sr-Substituted $MgFe_2O_4$ Nanoparticles at Different Calcination Temperatures. *Appl. Nanosci.*, 6, 629–639..

[43] Khandekar M S, Kambale R C, Patil J Y, Kolekar Y D & Suryavanshi S S (2011). Effect of Calcination Temperature on the Structural and Electrical Properties of Cobalt Ferrite Synthesized by Combustion Method. *J. Alloys Compd.*, 509, 1861–1865.

[44] Sheena P A, Priyanka K P, Sabu N Al, Sabu B & Varghese T (2014). Effect of Calcination Temperature on the Structural and Optical Properties of Nickel Oxide Nanoparticles. *Nanosyst. Physics, Chem. Math.*, 5, 441–449.

[45] Singh G, Jalandhara D & Yadav K (2016). Effect of Grain Size on Optical Properties of Iron Oxide Nanoparticles. *AIP Conference Proceeding*, vol 020409, pp 1–4.

[46] Indrayana I P T & Putra R A (2020). Pengaruh Konsentrasi Doping Zn^{2+} Terhadap Nilai Konstanta Optik Nanopartikel $Mn_{1-x}Zn_xFe_2O_4$ *J. Hadron*. 2, 5–15.

[47] Mukhtar W M, Halim R M, Dasuki K A, Rashid A R A & Taib N A M (2017). SPR Sensor for Detection of Heavy Metal Ions: Manipulating the EM Waves Polarization Modes. *Malaysian J. Fundam. Appl. Sci.*, 13, 619–622.